

Article

Three-Dimensional Hydrogen-Bonded Porous Metal-Organic Framework for Natural Gas Separation with High Selectivity

Wenyan Dan , Guangfeng Wei  and Xiangdong Fang 

College of Chemical Science and Engineering, Tongji University, 1239 Siping Road, Yangpu, Shanghai 200092, China

* Correspondence: wydan@tongji.edu.cn (W.D.); xdfang@tongji.edu.cn (X.F.)

Abstract: A 3D hydrogen-bonded metal-organic framework, [Cu(apc)₂]_n (TJU-Dan-5, Hapc = 2-aminopyrimidine-5-carboxylic acid), was synthesized via a solvothermal reaction. The activated TJU-Dan-5 with permanent porosity exhibits a moderate uptake of 1.52 wt% of hydrogen gas at 77 K. The appropriate BET surface areas and decoration of the internal polar pore surfaces with groups that form extensive hydrogen bonds offer a more favorable environment for selective C₂H₆ adsorption, with a predicted selectivity for C₂H₆/CH₄ of around 101 in C₂H₆/CH₄ (5:95, v/v) mixtures at 273 K under 100 kPa. The molecular model calculation demonstrates a C–H···π interaction and a van der Waals host–guest interaction of C₂H₆ with the pore walls. This work provides a strategy for the construction of 3D hydrogen-bonded MOFs, which may have great potential in the purification of natural gas.

Keywords: metal-organic frameworks; hydrogen bond; natural gas; separation



Citation: Dan, W.; Wei, G.; Fang, X.

Three-Dimensional Hydrogen-Bonded Porous Metal-Organic Framework for Natural Gas Separation with High Selectivity. *Molecules* **2024**, *29*, 424. <https://doi.org/10.3390/molecules29020424>

Academic Editor: Emilio Pardo

Received: 8 December 2023

Revised: 30 December 2023

Accepted: 8 January 2024

Published: 15 January 2024



Copyright: © 2024 by the authors. Licensee MDPI, Basel, Switzerland. This article is an open access article distributed under the terms and conditions of the Creative Commons Attribution (CC BY) license (<https://creativecommons.org/licenses/by/4.0/>).

1. Introduction

Metal-organic frameworks, as self-assembled porous materials, have been widely explored in the last two decades due to their excellent performance in the areas of gas storage and separation [1,2], heterogeneous catalysis [3], drug delivery [4], luminescence [5–7], electrochemistry [8], and magnetism [9]. The structure and properties of MOFs depend on the nature of their metal cations and bridging ligands. Designing MOFs with an eye for novel structures and utilities through the sagacious choice of various metal ions and ligands always constitutes one of the most intriguing research topics in chemistry and materials science [10–12]. Among the factors that may influence the structures of MOFs, hydrogen bonding is capable of providing overall structural rigidity and diversity [13], and the stability of the corresponding molecular networks can be enhanced by augmenting the number or strength of the hydrogen bonds in which each tectonic subunit participates [14]. However, hydrogen bonds are greatly affected by various factors, such as intermolecular distances, temperature, pressure, and solvents [15]. As a result, reports concerning the design and synthesis of functional MOFs involving both coordination bonds and hydrogen bonds are rather scarce in the chemical literature [16,17].

Three-dimensional hydrogen-bonded MOFs are usually assembled based on coordinated hydrogen bond interactions. According to the structural characteristics of reported 3D hydrogen-bonded MOFs, they can be constructed in three ways (Figure 1). The first is that the metal and ligand form a 0D cluster including an MOP (metalorganic polyhedron) or a macrocycle including MOCs (metal-organic cubes) and MOSs (metalorganic squares), which are further linked together along three directions to generate 3D frameworks [18–20]. Eddaoudi and Liu reported some hydrogen-bonded MOFs made with MOCs and MOSs [21–24] containing 3D hydrogen-bonding interactions. In this respect, MOC-2 and MOC-3, consisting of indium (III) and 4,5-dicyanoimidazole, were constructed from vertex-to-vertex hydrogen-bonded MOCs [21]. The second is that 1D chains of metal

and ligands are hydrogen-bonded along two orthogonal dimensions to give a 3D framework. Román synthesized a copper(II)-isophthalato MOF containing a 9-methyladenine nucleobase, exhibiting features of the second 3D hydrogen-bonded MOFs [25]. The last choice is similar to pillar-layered structures, in which the 2D networks of a metal and ligand are further interconnected by hydrogen bonds to generate 3D frameworks, as shown by $\{[\text{Zn}(\text{apc})_2] \cdot \text{H}_2\text{O}\}_n$ and DAT-MOF-1 [26,27].

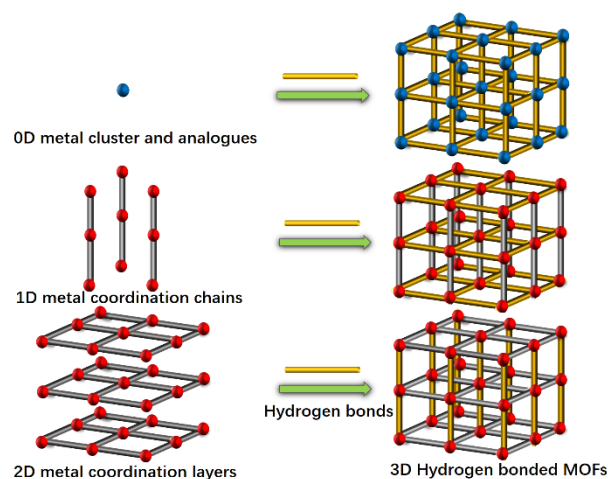


Figure 1. Schematic diagram showing the construction of 3D hydrogen-bonded MOFs in three ways (blue balls represent a metal cluster or macrocycle; the orange rods represent hydrogen bonds among ligands; red balls represent a metal or metal cluster; and the grey rods represent organic ligand parts).

However, great synthetic challenges still exist in constructing 3D hydrogen-bonded MOFs due to the less tunable character of hydrogen bonds. Using preorganized 2D metal organic sheets assembled by hydrogen bonds may be an alternative strategy to solve the above morass, albeit encountering the quandary of selecting suitable metal centers as well as ligands.

With recent developments in MOFs and HOFs (hydrogen-bonded organic frameworks), the separation properties of MOF and HOF materials have attracted considerable research and commercial interest based on the conception of CO_2 capture [28] and purification of natural gas [29], ethane [30], and butadiene [31]. In fact, the high porosities of materials are not prerequisites for their gas separation applications. As reported in the literature, MOFs and HOFs exhibiting excellent performance for gas separations are those of moderate porosities, with BET surface areas less than $1000 \text{ m}^2/\text{g}$ [32]. The design and synthesis of new porous MOF materials with hydrogen-bonding features may serve as a new concept to take advantage of the structural features of both materials with the aim of gas separation applications. Liu's group reported some hydrogen-bonded MOFs like ZSA-7, ZSA-8, and ZSA-9. ZSA-7 and ZSA-8 exhibit high CO_2 adsorption abilities (109.8 and $114.0 \text{ cm}^3 \cdot \text{g}^{-1}$ at 273 K , respectively, under 1 bar) and outstanding natural gas selectivity separation, especially for CO_2 over CH_4 (39.8 and 35.7 for $\text{CO}_2/\text{CH}_4 = 0.5/0.5$ and 76.0 and 51.6 for $\text{CO}_2/\text{CH}_4 = 0.05/0.95$, respectively, under 1 bar at 298 K) [33]. Natural gas is a hydrocarbon mixture primarily consisting of $85\% \text{ CH}_4$, $9\% \text{ C}_2\text{H}_6$, $3\% \text{ C}_3\text{H}_8$, $2\% \text{ N}_2$, and $1\% \text{ C}_4\text{H}_{10}$. To reduce the percentage of ethane content, it is very important to purify natural gas. With CH_4 as a premium choice for greenhouse effect reduction, using MOFs for the industrial separation of CH_4 and C_2H_6 in natural gas becomes urgent and necessary. As a fruitful approach, selectivity enhancements in gas separation have been successfully carried out through the precise control of the pore size and environment of MOFs [34]. However, the selectivity of C_2H_6 and CH_4 is low in the reported MOFs, and it may be due to the inappropriate BET surface areas and weak interactions of C_2H_6 with the cavity surface of the MOF frameworks [30,32]. In this respect, 3D hydrogen-bonded MOFs may be an excellent choice of porous materials for $\text{CH}_4/\text{C}_2\text{H}_6$ purification of natural gas.

Based on our preliminary study [26], we herein used the aminopyrimidylcarboxylate ligand (2-aminopyrimidine-5-carboxylic acid) and $\text{Cu}(\text{NO}_3)_2$ to deliver a 3D hydrogen bonded framework (namely **TJU-Dan-5**) through a solvothermal reaction, which consists of 2D **sql** networks connected by hydrogen bonds. The 1D permanent porosity of **TJU-Dan-5** exhibits higher $\text{C}_2\text{H}_6/\text{CH}_4$ selectivity (101:1, at 273 K/100 kPa) due to $\text{C-H}\cdots\pi$ interactions between C_2H_6 and the pore wall. In addition, **TJU-Dan-5** displays a high selectivity for equimolar $\text{C}_2\text{H}_6/\text{C}_2\text{H}_4$ mixture gas (selectivity: 2.46 at 298 K/100 kPa). This work demonstrates that internal hydrogen bonding implanted in the pore of MOFs provides both enhanced structural integrity and C_2H_6 friendly pore surfaces.

2. Results and Discussion

2.1. Structure Description

The crystallographic data and structure refinement information are listed in Table S1. **TJU-Dan-5**, $\text{Cu}(\text{apc})_2$, is crystallized in the monoclinic space group of $C2/c$. The asymmetric unit consists of one crystallographically independent Cu^{2+} ion and two molecules of apc^- ligand (Figure S1). As shown in Figure S2, the Cu^{2+} ion coordinates four carboxylate oxygen (Cu-O , 1.976(4) Å and 1.972(4), Table S2) and one pyrimidine nitrogen atom (Cu-N , 2.177(4) Å) has a distorted tetragonal pyramid conformation. The Hapc carboxylate groups coordinate the copper ion in a bidentate fashion (Figure S2), with the C-O bond distances of the carboxylate group ranging from 1.254(6) Å to 1.265(6) Å. Compared with the reported structure [26], Hapc adopted new coordination modes (III and IV, Figure S3). One apc ligand connects three copper ions through two Cu-O bonds and one Cu-N bond (mode IV, Figure S3). The other one apc ligand chelates two copper ions through two Cu-O bonds, and the aminopyrimidine group does not coordinate with copper ion (mode III, Figure S3). The free aminopyrimidine forms a hydrogen bond between amino and carboxylate instead ($d_{\text{N-H}\cdots\text{N}} = 2.988(6)$ Å, Figure S3 and Table S3). It is noteworthy that internal hydrogen bonds exist within aminopyrimidine groups ($d_{\text{N-H}\cdots\text{N}} = 2.984(6)$ Å, 3.051(7) Å, 3.054(6) Å, Figure S4 and Table S3).

The Cu paddle-wheel $\text{SBU}(\text{Cu}_2(\text{CO}_2)_2\text{N}_2)$ produced by two CuO_4N_1 tetrahedrons are corner-shared to form a 2D network along the a axis (Figure 2a, green). The other 2D network (Figure 2b, red) is also composed of Cu paddle-wheel SBU and a 1D helix chain along the b axis. A similar pillared-layer 3D framework is generated by internal hydrogen bonds among apc ligands of the 2D network (Figure 1, resulting in a one-dimensional hexagonal channel with the pore size of $5.0 \text{ \AA} \times 6.0 \text{ \AA}$ by the van der Waals radius along c axis (Figure 3). The void volume is 1272.9 \AA^3 (36.5%) as estimated by PLATON using a probe of 1.2 Å and the Connolly surface area is shown in Figure 4. Usually, 4, 4'-Bipyridine or analogue linker usually bridges the porous pillared-layer frameworks through coordination bonds [35]. However, the internal hydrogen bonds within aminopyrimidine groups link the 2D layers to construct the 3D porous pillar-layer network of **TJU-Dan-5**, the structure type rarely reported in MOFs. In contrast to most MOFs with metal ions or clusters coordinating with organic ligands, the framework of **TJU-Dan-5** provides a new example of 3D hydrogen-bonded MOFs (Figure 1). It is thus interesting to further explore the topology analysis of such hydrogen-bonded frameworks for the rational design of reticular chemistry of MOFs.

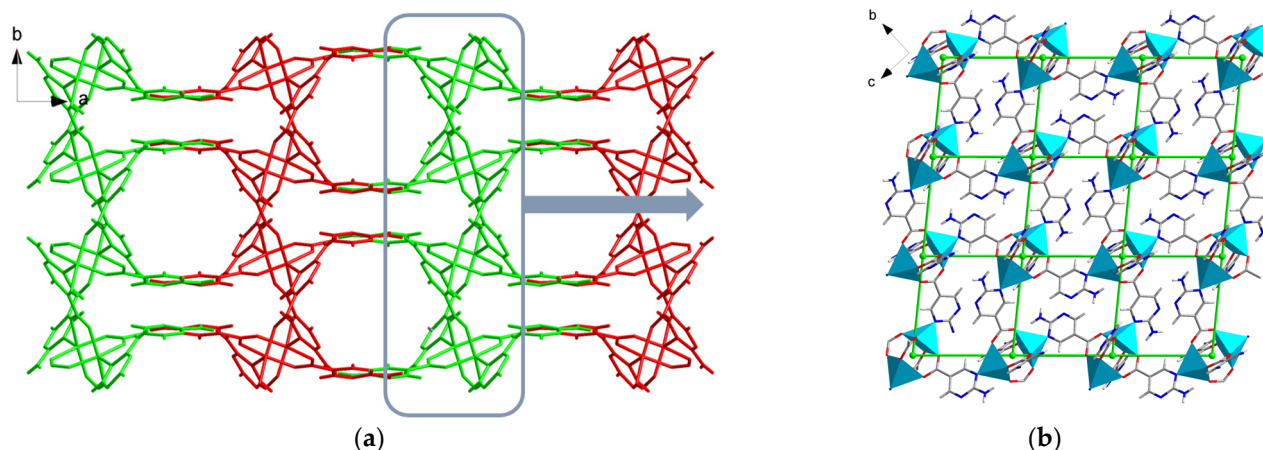


Figure 2. Structure of TJU-Dan-5. (a) Packing diagram of TJU-Dan-5 along c axis, (red: one two-dimensional coordination layer; green: the other two-dimensional coordination layers). (b) The two-dimensional layer can be simplified as sql topology (green grid) along a axis.

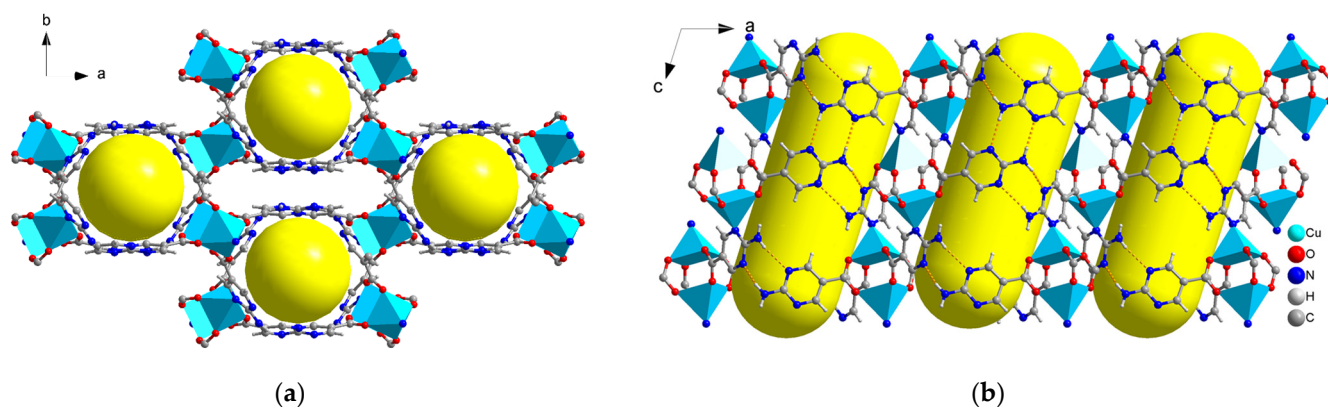


Figure 3. Packing view of TJU-Dan-5. (a) Yellow balls are added to highlight the porosity along c axis, (b) yellow columns are added to highlight the 1D channels, along b axis (C: dark gray; N: dark blue; O: red; H: light gray, $Cu_2(CO_2)_2N_2$: two light blue tetrahedrons). Hydrogen bonds within aminopyrimidine groups are represented in orange dotted lines.

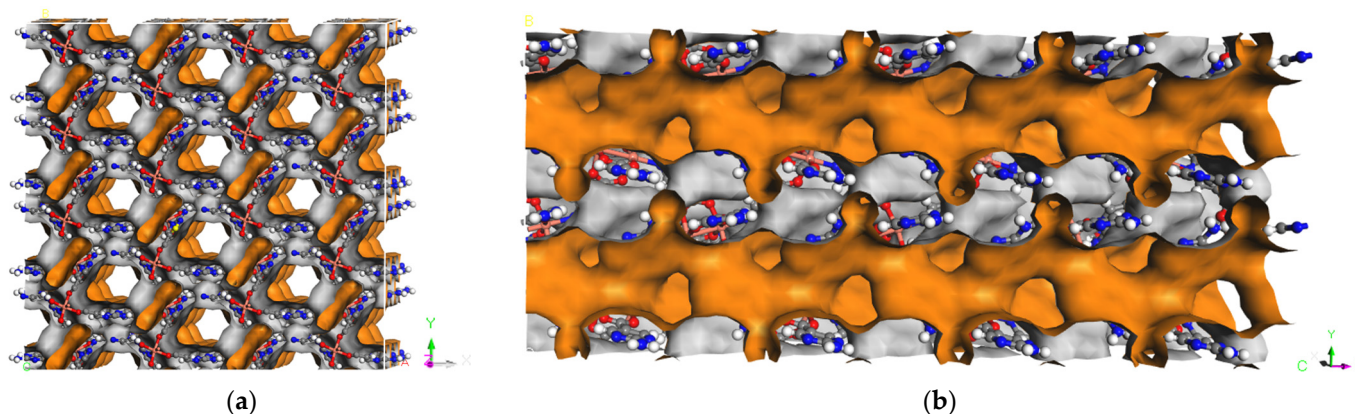


Figure 4. Connolly surface area (orange/grey curved surface) calculated with probe atomic radii of 1.4 \AA in TJU-Dan-5. (a) Along Z axis, (b) along X axis.

The topology of TJU-Dan-5 was analyzed by using the TOPOSPro program [36]. Firstly, the two-dimensional network formed by the metal cluster and ligands was investigated. Considering Cu paddle-wheel SBU($Cu_2(CO_2)_2N_2$) as a 4-connected node, each

layer yields a 2D 4-connected uninodal net with point symbol of $\{4^4.6^2\}$, which is a **sql** net (Figure 2b). Furthermore, hydrogen bonds participating in the 3D framework of **TJU-Dan-5** should be considered in the process of analyzing the topology. The two crystallographically independent apc^- ligands with different hydrogen bonds are regarded as two 3-connected nodes (Figure 5a), Cu paddle-wheel SBU ($Cu_2(CO_2)_2N_2$) as a 6-connected node, and the total 3-D network displays a trinodal (3,3,6)-connected net with point (Schläfli) symbol $\{6^3\}_4\{6^6.8^4.10^5\}$. According to the search results from the Reticular Chemistry Structure Resource (RCSR) database and the literature, only seven trinodal (3,3,6)-connected nets have been reported, including the symbol names of **brk**, **muo**, **tsa**, **tsy**, **xbq**, **zxc** [37], and another one with point symbols of $\{4^2.6\}\{4^3\}\{4^5.6^4.8^6\}$ [38]. Therefore, **TJU-Dan-5** provides a completely new topology in MOF crystal nets.

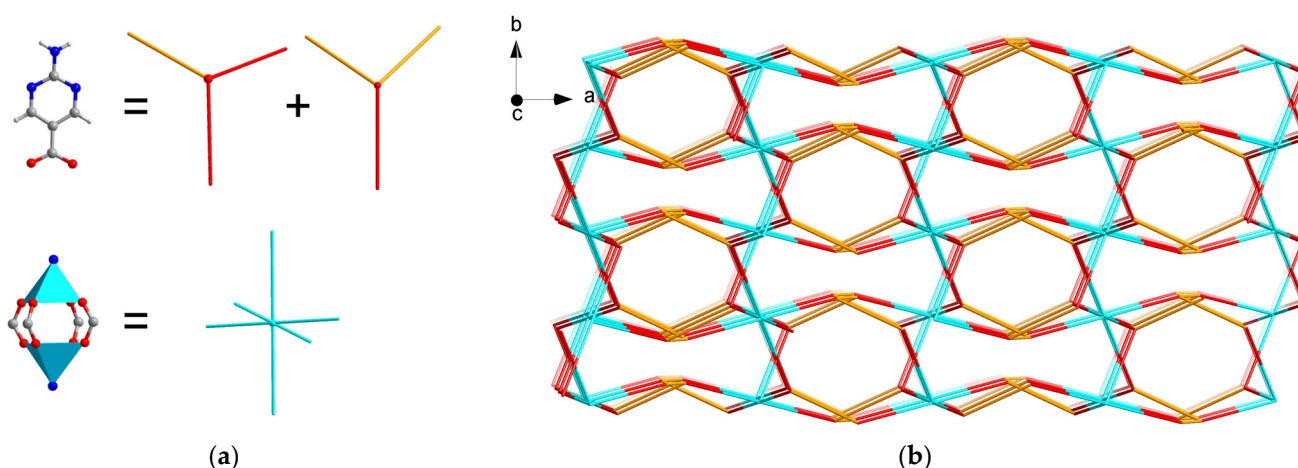


Figure 5. The simplified node and topology of **TJU-Dan-5**: (a) the simplified apc^- ligands in two 3-connected nodes (orange lines represent hydrogen bonds) and the simplified Cu paddle-wheel SBU $Cu_2(CO_2)_2N_2$ in 6-connected node; (b) the network of **TJU-Dan-5** showing in (3,3,6)-connected new topology.

2.2. Characterization of **TJU-Dan-5**

The thermal stability of **TJU-Dan-5** was further evaluated via a thermogravimetric analysis (TGA) and varied-temperature PXRD. A sharp weight loss above 270 °C in the TGA curve corresponded to the departure of the organic ligands and the collapse of the framework (Figure S5), while the varied-temperature PXRD patterns obtained at increasing temperatures show that the framework collapses above 270 °C (Figure S6). The framework of **TJU-Dan-5**, like most MOFs based Cu-paddle-wheel SBU, is stable up to 250 °C in air, both suggesting that hydrogen-bonded MOFs materials are structurally robust.

2.3. Gas Adsorption of H_2 and N_2

Adsorption experiments were thus carried out to evaluate the rigidity and permanent porosity of **TJU-Dan-5**. The N_2 sorption at 77 K for activated **TJU-Dan-5** shows type I adsorption isothermal behavior, characteristic of a microporous material with permanent porosity (Figures S7 and S8). The Brunauer–Emmett–Teller (BET) and Langmuir surface area of **TJU-Dan-5** were determined to be $748.7 \text{ m}^2 \cdot \text{g}^{-1}$ and $914.2 \text{ m}^2 \cdot \text{g}^{-1}$, respectively. The experimental pore volume was calculated to be $0.323 \text{ cm}^3 \cdot \text{g}^{-1}$. The pore size distribution of **TJU-Dan-5**, analyzed by the NLDFT model, displays a peak of 6.0 \AA in the micropore region, which is close to the size of the hexagonal channel in the crystal structure of title compound (Figure S7, inset). Hydrogen adsorption reveals a moderate uptake of 1.52 wt% at 77 K (1 atm) (Figure S9). **TJU-Dan-5** may be studied as a potential hydrogen storage material. The $Q_{st}(H_2)$ is slightly lower than that of MOF-74(Zn) but considerably higher than those of other porous materials, such as MOF-177, JUC-48, and PCN-17 [39]. The

isosteric heat of H_2 sorption, calculated by fitting the adsorption data at 77 K and 87 K to the Virial equation, was found to be 7.98 kJ/mol at zero coverage (Figures S10 and S11).

2.4. Separations of C_2H_6/CH_4 and C_2H_6/C_2H_4

Separation of C_2H_6 from natural gas is crucial in sufficient utilization of natural gas and CO_2 reduction in the earth atmosphere. The unique channel sizes of **TJU-Dan-5** us to investigate its potential in the C_2H_6/CH_4 separation from natural gas. In this respect, single-component sorption isotherms of CH_4 and C_2H_6 were measured at 273 K and 298 K, respectively. For **TJU-Dan-5**, the absorbed amounts of CH_4 at 273 and 298 K are only 23.6 and 15.2 $cm^3 \cdot g^{-1}$, respectively (Figure 6), whereas the corresponding C_2H_6 amounts of gas uptake at 273 and 298 K are 50.3 and 45.03 $cm^3 \cdot g^{-1}$ (Figure 6). More importantly, under low pressure below 30 kPa, **TJU-Dan-5** takes up much more C_2H_6 than CH_4 . **TJU-Dan-5** takes up a much different amount of C_2H_6 and CH_4 , suggesting of separation selectivity of **TJU-Dan-5** in C_2H_6 and CH_4 . In addition, C_2H_2 , C_2H_4 , and CO_2 gas sorption isotherms of **TJU-Dan-5** were measured at 273 K and 298 K, respectively (Figure 7). **TJU-Dan-5** can take up the amounts of 57.79 $cm^3 \cdot g^{-1}$ and 50.06 $cm^3 \cdot g^{-1}$ for C_2H_2 , 47.86, 41.64 $cm^3 \cdot g^{-1}$ and 36.25 $cm^3 \cdot g^{-1}$ for C_2H_4 , and 59.27 $cm^3 \cdot g^{-1}$ and 36.25 $cm^3 \cdot g^{-1}$ for CO_2 at different temperature levels (Figure 4).

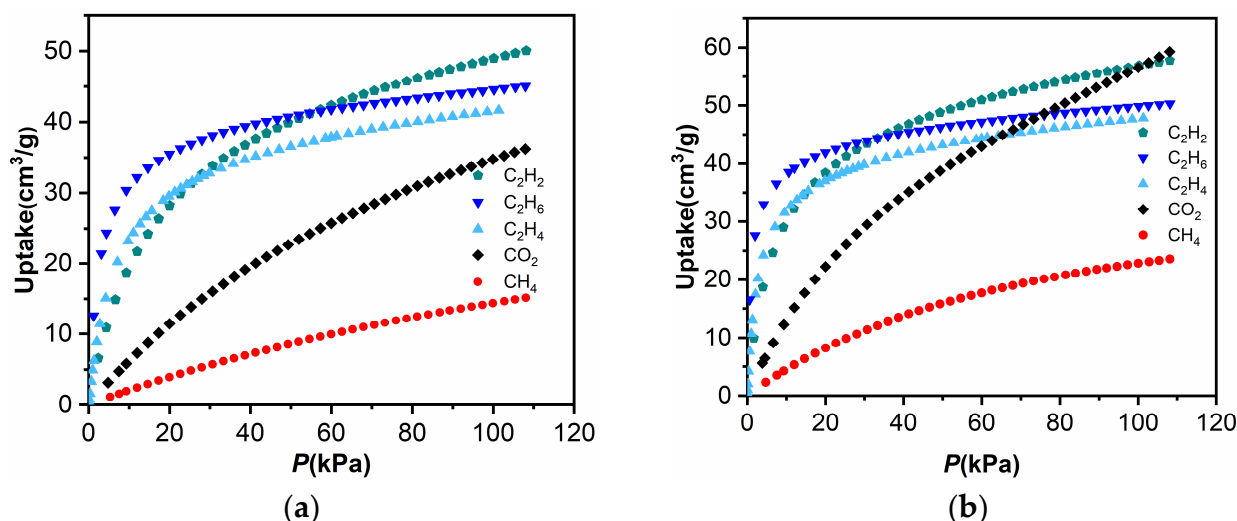


Figure 6. CO_2 , CH_4 , C_2H_2 , C_2H_4 , and C_2H_6 adsorption isotherms for **TJU-Dan-5** measured at 298 K (a) and 273 K (b).

To obtain binding energy at low coverage, isosteric adsorption heats of C_2H_6 , CH_4 , C_2H_2 , and C_2H_4 for **TJU-Dan-5** were calculated through the Virial equation and using the Clausius–Clapeyron relation, respectively (Figures S12 and S13). As shown in Figure S12, the isosteric adsorption heat of C_2H_6 is higher than the others. At zero coverage of C_2H_6 interaction with the most energetically favored adsorption sites, the enthalpy of 35.5 $kJ \cdot mol^{-1}$ can be attributed to stronger van der Waals host–guest interactions and $C-H \cdots \pi$ interaction between **TJU-Dan-5** and C_2H_6 . Pyridine rings presented in **TJU-Dan-5** may bring C_2H_6 in close contact with the pore walls. To visualize the preferential binding sites of C_2H_6 , DFT-based structural potential energy surface searching identified strong $C-H \cdots \pi$ interactions between C_2H_6 and the framework (the distances between H and pyrimidine centroids: 2.76 and 3.25 Å in Figure 7) and van der Waals host–guest interaction (the nearest distances between H and pyrimidine: 2.61 and 2.81 Å in Figure 7). In fact, the calculated adsorption energy of C_2H_6 on **TJU-Dan-5** is 34.7 kJ/mol, in an excellent agreement with the experimental data.

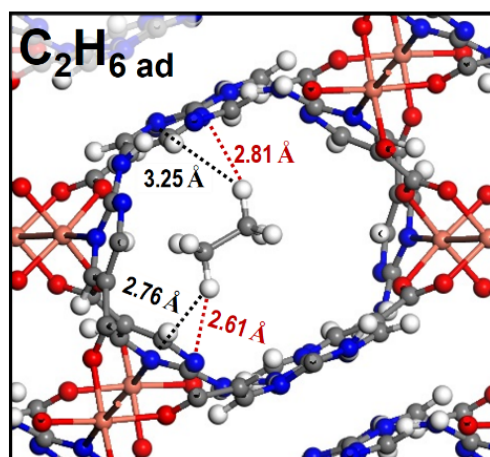


Figure 7. DFT-calculated optimized C_2H_6 adsorption site, van de Waals host-guest interactions (red dotted lines), and $C-H \cdots \pi$ interaction (black dotted lines) C_2H_6 and **TJU-Dan-5**. Color codes: Cu, pink; C, gray; H, white; O, red; and N, blue.

The ideal adsorbed solution theory (IAST) is used to calculate C_2H_6/CH_4 , C_2H_6/C_2H_4 , C_2H_2/CH_4 [40] and gas mixture selectivity respectively (see the Supporting information, Equations (S1) and (S2)). **TJU-Dan-5** shows the selectivity of C_2H_6/CH_4 (68 at 50:50), C_2H_6/CH_4 (67 at 5:95), 298 K (100 kPa); C_2H_6/CH_4 (146 at 50:50), C_2H_6/CH_4 (101 at 5:95), 273 K (100 kPa); C_2H_2/CH_4 (15 at 50:50), 298 K (100 kPa); C_2H_2/CH_4 (25 at 50:50), 273 K (100 kPa) (Figure 8). In the calculation, **TJU-Dan-5** exhibits greater separation ratios of C_2H_6/CH_4 at both 273 K and 298 K. The high selectivities of **TJU-Dan-5** in C_2H_6/CH_4 separation are better than those of MOFs or HOFs (Table 1) reported at room temperature, such as FJI-C4 [41], UTSA-33 [42], SNNU-Bai67 [43], VNU-18 [44], SBMOF-2, and HOF-BTB [45,46]. These results may be attributed to the stronger affinity between the pore environment of **TJU-Dan-5** and C_2H_6 , making **TJU-Dan-5** a good choice for natural gas purification. In addition, it is worth noting that the selectivity for C_2H_6/C_2H_4 equimolar mixtures is 2.46 at 298 K (100 kPa) (Figure 9), only lower than some leading MOFs in gas separation, such as MAF-49 (2.9) [30], Zn-FBA (2.9) [47], Cu(Qc)₂ (3.4) [48], and Fe₂(O₂)(dobdc) (4.4) [49], supporting our prediction of **TJU-Dan-5** utilization in gas separation.

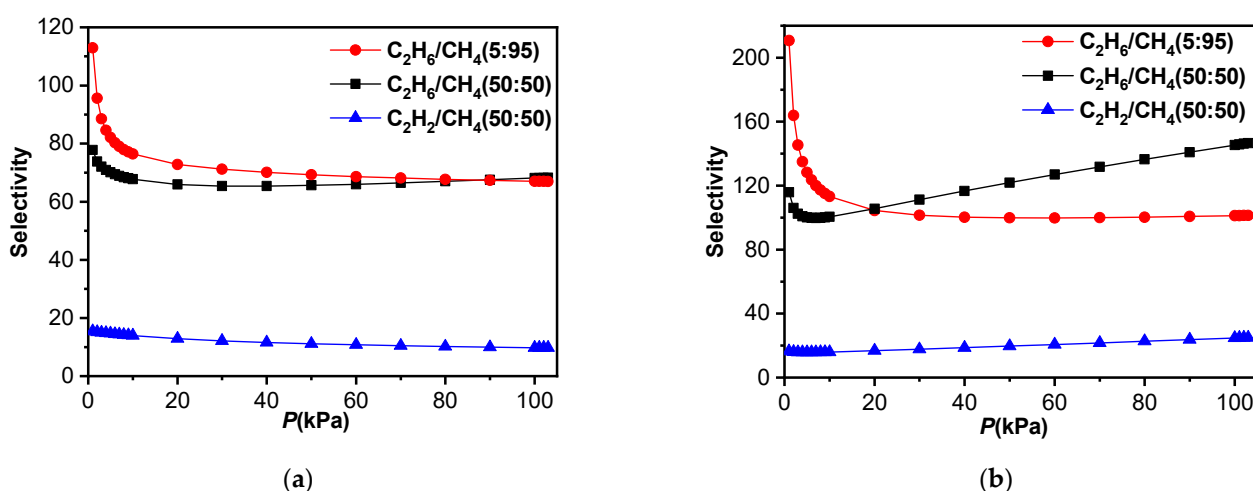


Figure 8. Selectivity predicted via DSLF-IAST method for adsorption of equimolar binary mixture (C_2H_2/CH_4 , CH_4/C_2H_6) in **TJU-Dan-5** at 298 K (a) and 273 K (b).

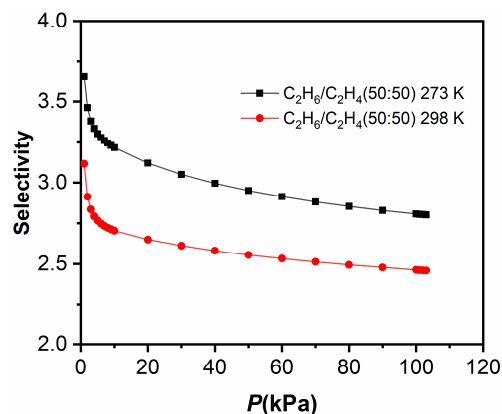


Figure 9. Selectivity predicted via DSLF-IAST method for adsorption of equimolar binary mixture C_2H_6/C_2H_4 in **TJU-Dan-5** at 298 K and 273 K.

Table 1. Comparison of some typical MOFs and HOF for the separation of C_2H_6/CH_4 and C_2H_2/CH_4 as predicted by IAST.

MOF	BET	C_2H_6/CH_4 (50:50)	C_2H_6/CH_4 (5:95)	C_2H_2/CH_4 (50:50)	T (K)	Gas Uptake C_2H_6 & CH_4	Refs.
TJU-Dan-5 *	748	146.5 68	101.2 67	25.0 15.4	273 298	50.3/23.6 45.03/15.2	This work This work
UTSA-35 *	742.7	15	/	19	296	51/9	[50]
$[Co_2(5,4-PMIA)_2(TPOM)_{0.5}]$	920	34.7	/	32.0	300	81.9/16.9	[51]
FJI-C4 *	690	39.7	/	51	298	66.3/18.4	[41]
UTSA-33 *	660	20	/	17.1	296	59/12	[42]
Cu-TDPAT	1938	16.4 12.1	/ /	154.3 127.1	273 298	217.7/51.6 154.4/28.3	[52] [52]
JLU-MOF112 *	1553	12	24	/	298	107.7/10.2	[29]
SNNU-Bai67	989.5	38.3	/	50.5	298	91.2/15.8	[43]
VNU-18	900	27.3	/	41.5	298	72.8/18.5	[44]
SBMOF-2	195	26	/	18	298	59.8/16.2	[45]
ZJNU-119 *	950	20.9	/	62.9	298	89.2/37.5	[53]
HOF-BTBa	955	17.7 13.7	/	12.5 9.3	273 295	95.4/13.44 69.2/10.08	[46] [46]
PFC-5 *	256	19	/	15	298	25.9/8.0	[54]
HOF-14	2573	6.3	/	3.7	298	44.2/7.8	[55]
MAF-49		170	/	/	316	36/22	[30]
$[Zn_2(bdc)_2(bpndi)]$	565	175	/	496	298	44/8	[56]

* The selectivity value at 1 bar.

Dynamic breakthrough experiments toward C_2H_6/CH_4 (5:95, *v/v*) and C_2H_6/C_2H_4 (50:50, *v/v*) were carried out at 298 K (Figure 10). The activated **TJU-Dan-5** sample was packed into a column, with the binary gas mixtures of CH_4/C_2H_6 and C_2H_4/C_2H_6 flowing at 5.0 mL min^{-1} at room temperature. As shown in Figure 10a, CH_4 was immediately monitored in the outlet of the fixed bed, while the C_2H_6 was retained in the column packed with **TJU-Dan-5** for 70 min/g. The results demonstrate that **TJU-Dan-5** is capable of trapping C_2H_6 molecules from CH_4/C_2H_6 mixtures. High-purity CH_4 products ($\geq 99.99\%$) can be directly obtained, and during the time of 0 to 66 min/g (C_2H_6 does not reach

its breakthrough point), the amounts of CH_4 captured in **TJU-Dan-5** were calculated to be 299.31 mL/g. In Figure 10b, C_2H_4 was eluted from a column before C_2H_6 with different retention times of 7.5 and 10.3 $\text{min}\cdot\text{g}^{-1}$, respectively, in an equimolar mixture. The purity of CH_4 was determined to be $\geq 99.04\%$. The breakthrough curves are kept over three cycles, indicating that the sample is sufficiently stable at the given conditions. In addition, the PXRD experiments further confirm the working stability of **TJU-Dan-5** following the sorption experiments and breakthrough tests (Figure S14). Separation of absolute C_2H_6 from $\text{CH}_4/\text{C}_2\text{H}_6$ mixture can be achieved by using activated **TJU-Dan-5** under ambient conditions.

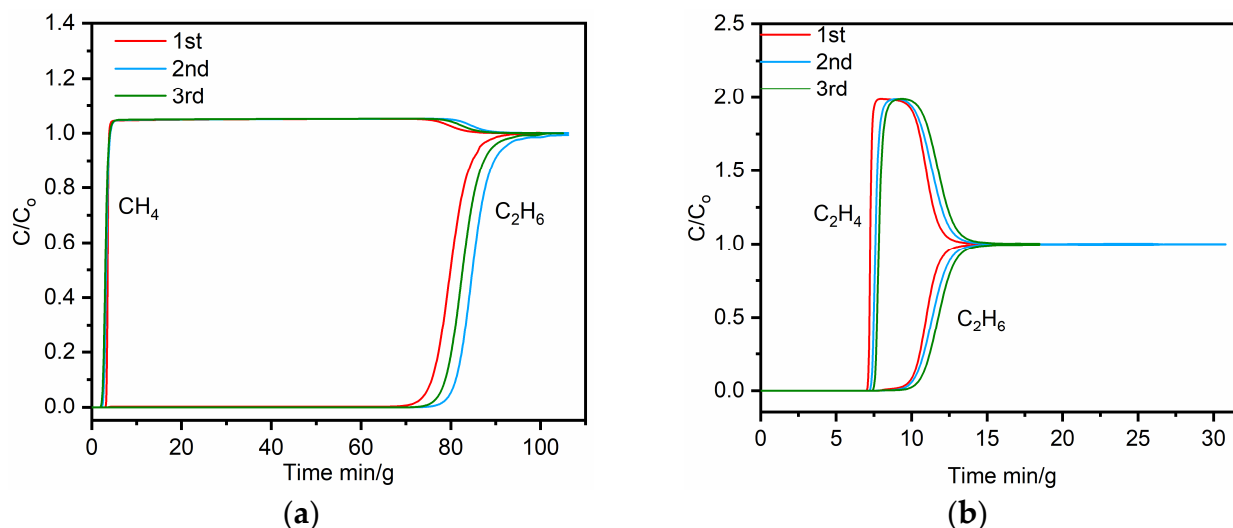


Figure 10. Experimental column breakthrough curves of **TJU-Dan-5**. (a) $\text{CH}_4/\text{C}_2\text{H}_6$ (5/95) mixture under a flow of $5 \text{ mL}\cdot\text{min}^{-1}$, (b) $\text{C}_2\text{H}_4/\text{C}_2\text{H}_6$ (50/50) mixture under a flow of $5 \text{ mL}\cdot\text{min}^{-1}$ in an absorber bed packed with **TJU-Dan-5** at 298 K and 1.0 bar. (The results were individually tested three times).

3. Materials and Methods

3.1. General Materials and Methods

All reagents for syntheses were purchased from commercial sources. Thermogravimetric (TGA) analyses were investigated with a Mettler Toledo TGA/SDTA851 analyzer (Mettler Toledo, Zurich, Switzerland) in N_2 atmosphere with a heating rate of $5 \text{ K}\cdot\text{min}^{-1}$, from $30 \text{ }^\circ\text{C}$ to $800 \text{ }^\circ\text{C}$. Elemental analyses (C, N, H) were measured on an Elementar Vario EL III microanalyzer (Elementar, Frankfurt, Germany). IR spectra were measured from a KBr pellets on a Thermo Scientific Nicolet IS10 FT-IR spectrometer (Thermo Scientific, Waltham, MA, USA) in the range of $4000\text{--}400 \text{ cm}^{-1}$. Powder X-ray diffraction (PXRD) patterns were carried out using a Bruker D8 powder diffractometer (Bruker, Karlsruhe, Germany) at 40 kV, 40 mA for Cu $\text{K}\alpha$ radiation ($\lambda = 1.5406 \text{ \AA}$), with a scan speed of 0.2 s/step and a step size of 0.05° (2θ).

3.2. Synthesis of **TJU-Dan-5**

$[\text{Cu}(\text{apc})_2]_n$ (**TJU-Dan-5**, Hapc = 2-aminopyrimidine-5-carboxylic acid) was obtained via solvothermal synthesis. A mixture of Hapc (0.014 g, 0.1 mmol), $\text{Cu}(\text{NO}_3)_2\cdot 3\text{H}_2\text{O}$ (0.013 g, 0.06 mmol), DMF (2.0 mL), and anhydrous methyl alcohol (0.5 mL) was placed in a 10 mL glass bottle and stirred for 1 h at room temperature. After the mixture was sealed in a Pyrex tube and heated at $60 \text{ }^\circ\text{C}$ for 2 days, the whole apparatus was cooled to room temperature. Blue plate crystals of **TJU-Dan-5** were collected via filtration (yield: 55% based on $\text{Cu}(\text{NO}_3)_2\cdot 3\text{H}_2\text{O}$). Elemental analysis (%): calcd. for $[\text{Cu}(\text{apc})_2]_n$ (339.75): C 35.35, H 2.37, N 24.74; found: C 35.41, H 2.50, N 24.60. IR (KBr, cm^{-1}): 3401 cm^{-1} (m), 3303 cm^{-1} (w), 1686 cm^{-1} (w), 1646 cm^{-1} (w), 1601 cm^{-1} (m), 1508 cm^{-1} (w), 1414 cm^{-1}

(m), 1357 cm⁻¹ (m), 1246 cm⁻¹ (w), 1181 cm⁻¹ (w), 1084 cm⁻¹ (m), 1003 cm⁻¹ (w), 844 cm⁻¹ (m), 810 cm⁻¹ (w), 683 cm⁻¹ (w), 602 cm⁻¹ (w), 477 cm⁻¹ (m).

3.3. X-ray Crystallography

The data for **TJU-Dan-5** were collected from a single crystal at 296(2) K on a Bruker D8 VENTURE dual-wavelength Mo/Cu three-circle diffractometer with a microfocus sealed X-ray tube using mirror optics as monochromator and a Bruker PHOTON II detector (Bruker, Karlsruhe, Germany). MoK α radiation ($\lambda = 0.71073 \text{ \AA}$) was MoK α used in the diffractometer. All data were integrated with SAINT and a multi-scan absorption correction using SADABS was applied [57,58]. The structure was solved by direct methods using SHELXT and refined by full-matrix least-squares methods against F^2 by SHELXL-2019/1 [59,60]. All non-hydrogen atoms were refined with anisotropic displacement parameters. The hydrogen atoms were refined isotropically on calculated positions using a riding model with their Uiso values constrained to 1.5 times the Ueq of their pivot atoms for terminal sp³ carbon atoms and 1.2 times for nitrogen and all other carbon atoms. The crystallographic data for the structures reported in this paper have been deposited with the Cambridge Crystallographic Data Centre [61]. CCDC 1830585 for **TJU-Dan-5** includes the supplementary crystallographic data for this paper. These data can be acquired free of charge via www.ccdc.cam.ac.uk/data_request/cif (accessed on 21 April 2020), or by emailing data_request@ccdc.cam.ac.uk, or by contacting The Cambridge Crystallographic Data Centre, 12, Union Road, Cambridge CB2 1EZ, UK; fax: +44 1223 336033. This report and the CIF file were generated using FinalCif [62].

3.4. Gas Adsorption Measurements

The as-synthesized materials of **TJU-Dan-5** were washed with DMF and CH₃OH for three times, respectively. Solvent was exchanged with CH₂Cl₂ for nine times over three days. CH₂Cl₂ was further removed with supercritical liquid CO₂ in a Tousimis Samdri PVT-30 critical point dryer (Tousimis, Rockville, MD, USA). N₂ adsorption and desorption measurements were measured on a Quantachrome Autosorb-iQ gas adsorption analyzer (Quantachrome, Tallahassee, FL, USA) and pore size analyzer at 77 K. The pore size distribution of **TJU-Dan-5** was analyzed by the NLDFT model utilizing N₂ adsorption data at 77 K (calculation model: N₂ at 77 K on carbon (slit/cylinder. pore, NLDFT equilibrium model); Eff. mol. Diameter (D): 3.54 \AA). Before the gas adsorption tests, the experimental sample was immersed in CH₃OH for 36 h, and then the exchanged sample was activated under vacuum at 100 °C for 10 h. Single H₂ sorption experiments were measured on a Micromeritics ASAP 2020 adsorption analyzer (Micromeritics, Atlanta, GA, USA) at 77 K and 87 K via liquid N₂ bath and liquid Ar bath, respectively. C₂H₆, C₂H₂, C₂H₄, CH₄ and CO₂ absorption experiments were performed on the Micromeritics ASAP 2020 adsorption analyzer at 273 K and 298 K via an ice-water bath and heating jacket, respectively. Two different temperatures isotherms were fitted to the Virial model and the isosteric heats of C₂H₆, C₂H₄, C₂H₂, and CH₄ adsorption were calculated, respectively. The selectivity of C₂H₆ and C₂H₂ over CH₄ was calculated with the ideal adsorbed solution theory (IAST) model (Equations (S1) and (S2)) at 273 K and 298 K.

3.5. Breakthrough Measurements

The breakthrough experiment was carried out using a multi-constituent adsorption breakthrough curve analyzer (BSD-MAB, Beishide Instrument Technology (Beijing) Co., Ltd., No. 607, Building 1, Brilliant International, Shangdi 10th Street, Haidian District, Beijing, China). The gas separation properties of **TJU-Dan-5** (1.26 g) were examined by breakthrough experiments using 0.05 (C₂H₆): 0.95 (CH₄) and 0.5 (C₂H₆): 0.5 (C₂H₄) gas mixtures flowing through the activated samples packed into the same glass column (6.0 mm inner diameter, 65 mm in length), respectively. The gas mixture passed through the column at a rate of 5 mL/min. The composition of the effluent gas was detected by a Mass spectrometry.

3.6. Density Functional Theory Calculations

Spin polarized density functional theory (DFT) calculations were performed using VASP packages with projected augmented wave (PAW) pseudo-potentials [63–65]. The exchange–correlation energy was treated based on the generalized gradient approximation (GGA) by using Perdew–Burke–Ernzerhof (PBE) functional [66]. The plane-wave cutoff energy was set to 450 eV. Brillouin zone sampling was restricted to the Gamma point [67]. The DFT-D3(BJ) method of Grimme were employed to describe long-range vdW interactions [68,69]. In this work, the crystal structure of the **TJU-Dan-5** framework was obtained according to the experimental characterization results. The optimized lattice parameters of **TJU-Dan-5** are $11.13 \text{ \AA} \times 13.34 \text{ \AA} \times 13.16 \text{ \AA}$, with $\alpha = 106.74^\circ$, $\beta = 90.01^\circ$, $\gamma = 65.39^\circ$, which are close to the experimental characterization results. The preferential binding sites of small molecules were searched via the stochastic surface walking (SSW) method [70,71], which has been implemented in a computing program (LASP www.lasphub.com (accessed on 21 July 2022)). LASP is now available on market, and it can interface with VASP for all the functionalities. All atoms were fully relaxed during the lattice optimization. The Quasi-Newton I-BFGS method is used for geometry relaxation until the maximal force on each degree of freedom is less than 0.05 eV/\AA .

4. Conclusions

A new 3D hydrogen bonding MOF (**TJU-Dan-5**) was successfully synthesized and characterized. As observed in the solid-state structure, two 2D metal coordination planes of **TJU-Dan-5** were ligated by hydrogen bonds, resulting in a 1D porous channel. Albeit no open metal site in **TJU-Dan-5**, the permanent porosity of **TJU-Dan-5** results in moderate performance for adsorption of H_2 gas as well as high $\text{C}_2\text{H}_6/\text{CH}_4$ and $\text{C}_2\text{H}_6/\text{C}_2\text{H}_4$ selectivity. The molecular model calculation result reveals strong $\text{C-H}\cdots\pi$ interactions between C_2H_6 and the pore wall, suggesting intermolecular hydrogen bonding in favor of pore integrity and C_2H_6 selection. We are exploring the possibility of diversifying the 3D hydrogen-bonded MOFs family for gas separation and further developing this synthetic concept.

Supplementary Materials: The following supporting information can be downloaded at: <https://www.mdpi.com/article/10.3390/molecules29020424/s1>, Figure S1: The asymmetric unit of compound **TJU-Dan-5**; Figure S2: The coordinated environment around the metal center of **TJU-Dan-5**; Figure S3: The coordination mode of Hapc; Figure S4: Hydrogen bonds in **TJU-Dan-5**; Figure S5: TGA curve of active **TJU-Dan-5**; Figure S6: XRD patterns of **TJU-Dan-5** in air from room temperature to 270°C ; Figure S7: Nitrogen sorption isotherm of **TJU-Dan-5** at 77 K; Figure S8: BET surface area plot for **TJU-Dan-5**; Figure S9: Hydrogen sorption isotherm of **TJU-Dan-5**; Figure S10: Isothermic heat of adsorption Q_{st} of H_2 for **TJU-Dan-5**; Figure S11: The H_2 isotherms at 77 K and 87 K and the Virial equation fits for **TJU-Dan-5**; Figure S12: Isothermic heat of adsorption Q_{st} of C_2H_6 , C_2H_4 , C_2H_2 , CH_4 for **TJU-Dan-5**; Figure S13: The gas isotherms at 273 K and 298 K and the Virial equation fits for **TJU-Dan-5**; Figure S14: PXRD patterns of **TJU-Dan-5** after sorption experiments and breakthrough tests; Table S1: Crystal data and structure refinement of **TJU-Dan-5**; Table S2: Selected bond lengths (\AA) and angles ($^\circ$) for **TJU-Dan-5**; Table S3: Hydrogen bonds for **TJU-Dan-5**; Table S4: Parameters for DSLF isotherm fits at 298 K.

Author Contributions: Writing—original draft, W.D.; investigation, W.D.; data curation, W.D.; software, G.W.; methodology, W.D.; resources, W.D.; writing—review and editing, W.D. and X.F. All authors have read and agreed to the published version of the manuscript.

Funding: This work was supported by National Natural Science Foundation of China (Grant Number: 21971195), the Research Project of Shanghai Science and Technology Commission (Grant number: 21ZR1467800), and the Fundamental Research Funds for the Central Universities (Grant Number: C1-22120180252).

Institutional Review Board Statement: Not applicable.

Informed Consent Statement: Not applicable.

Data Availability Statement: Data are contained within the article and Supplementary Material.

Acknowledgments: We are extremely grateful to Guiyang Zhang and Binbin Tu for help with gas adsorption determination; to Yanfeng Bi and Jia Li for help with selective calculations; and to Xin Xu for valuable discussion.

Conflicts of Interest: The authors declare no conflicts of interest.

References

1. Li, J.R.; Sculley, J.; Zhou, H.C. Metal-organic frameworks for separations. *Chem. Rev.* **2012**, *112*, 869–932. [[CrossRef](#)]
2. He, Y.; Zhou, W.; Qian, G.; Chen, B. Methane storage in metal-organic frameworks. *Chem. Soc. Rev.* **2014**, *43*, 5657–5678. [[CrossRef](#)] [[PubMed](#)]
3. Liu, J.; Chen, L.; Cui, H.; Zhang, J.; Zhang, L.; Su, C.Y. Applications of metal-organic frameworks in heterogeneous supramolecular catalysis. *Chem. Soc. Rev.* **2014**, *43*, 6011–6061. [[CrossRef](#)]
4. Della Rocca, J.; Liu, D.; Lin, W. Nanoscale Metal-organic frameworks for biomedical imaging and drug delivery. *Acc. Chem. Res.* **2011**, *44*, 957–968. [[CrossRef](#)]
5. Hu, Z.; Deibert, B.J.; Li, J. Luminescent metal-organic frameworks for chemical sensing and explosive detection. *Chem. Soc. Rev.* **2014**, *43*, 5815–5840. [[CrossRef](#)] [[PubMed](#)]
6. Yin, J.; Li, W.; Li, W.; Liu, L.; Zhao, D.; Liu, X.; Hu, T.; Fan, L. Heterometallic ZnHoMOF as a dual-responsive luminescence sensor for efficient detection of hippuric acid biomarker and nitrofurantoin antibiotics. *Molecules* **2023**, *28*, 6274. [[CrossRef](#)] [[PubMed](#)]
7. Li, W.; Li, W.; Liu, X.; Zhao, D.; Liu, L.; Yin, J.; Li, X.; Zhang, G.; Fan, L. Two chemorobust cobalt(II) organic frameworks as high sensitivity and selectivity sensors for efficient detection of 3-nitrotyrosine biomarker in serum. *Cryst. Growth Des.* **2023**, *23*, 7716–7724. [[CrossRef](#)]
8. Xiao, X.; Zou, L.; Pang, H.; Xu, Q. Synthesis of micro/nanoscaled metal-organic frameworks and their direct electrochemical applications. *Chem. Soc. Rev.* **2020**, *49*, 301–331. [[CrossRef](#)]
9. Kurmoo, M. Magnetic metal-organic frameworks. *Chem. Soc. Rev.* **2009**, *38*, 1353–1379. [[CrossRef](#)]
10. Kitagawa, S.; Kitaura, R.; Noro, S.-I. Functional porous coordination polymers. *Angew. Chem. Int. Ed.* **2004**, *43*, 2334–2375. [[CrossRef](#)]
11. Furukawa, H.; Cordova, K.E.; O’Keeffe, M.; Yaghi, O.M. The chemistry and applications of metal-organic frameworks. *Science* **2013**, *341*, 1230444. [[CrossRef](#)]
12. Lu, W.; Wei, Z.; Gu, Z.Y.; Liu, T.F.; Park, J.; Park, J.; Tian, J.; Zhang, M.; Zhang, Q.; Gentle Iii, T.; et al. Tuning the structure and function of metal-organic frameworks via linker design. *Chem. Soc. Rev.* **2014**, *43*, 5561–5593. [[CrossRef](#)] [[PubMed](#)]
13. Li, Z.T.; Wu, L.Z. *Hydrogen Bonded Supramolecular Structures*; Springer: Berlin/Heidelberg, Germany, 2015; p. 87.
14. Brunet, P.; Simard, M.; Wuest, J.D. Molecular Tectonics. Porous hydrogen-bonded networks with unprecedented structural integrity. *J. Am. Chem. Soc.* **1997**, *119*, 2737–2738. [[CrossRef](#)]
15. Lin, R.B.; He, Y.; Li, P.; Wang, H.; Zhou, W.; Chen, B. Multifunctional porous hydrogen-bonded organic framework materials. *Chem. Soc. Rev.* **2019**, *48*, 1362–1389. [[CrossRef](#)] [[PubMed](#)]
16. Thomas-Gipson, J.; Beobide, G.; Castillo, O.; Fröba, M.; Hoffmann, F.; Luque, A.; Pérez-Yáñez, S.; Román, P. Paddle-wheel shaped copper(II)-adenine discrete entities as supramolecular building blocks to afford porous supramolecular metal-organic frameworks (SMOFs). *Cryst. Growth Des.* **2014**, *14*, 4019–4029. [[CrossRef](#)]
17. Thomas-Gipson, J.; Pérez-Aguirre, R.; Beobide, G.; Castillo, O.; Luque, A.; Pérez-Yáñez, S.; Román, P. Unravelling the growth of supramolecular metal-organic frameworks based on metal-nucleobase entities. *Cryst. Growth Des.* **2015**, *15*, 975–983. [[CrossRef](#)]
18. Beobide, G.; Castillo, O.; Cepeda, J.; Luque, A.; Pérez-Yáñez, S.; Román, P.; Thomas-Gipson, J. Metal-carboxylato-nucleobase systems: From supramolecular assemblies to 3D porous materials. *Coord. Chem. Rev.* **2013**, *257*, 2716–2736. [[CrossRef](#)]
19. An, J.; Fiorella, R.P.; Geib, S.J.; Rosi, N.L. Synthesis, structure, assembly, and modulation of the CO₂ adsorption properties of a zinc-adeninate macrocycle. *J. Am. Chem. Soc.* **2009**, *131*, 8401–8403. [[CrossRef](#)]
20. Nugent, P.S.; Rhodus, V.L.; Pham, T.; Forrest, K.; Wojtas, L.; Space, B.; Zaworotko, M.J. A robust molecular porous material with high CO₂ uptake and selectivity. *J. Am. Chem. Soc.* **2013**, *135*, 10950–10953. [[CrossRef](#)]
21. Sava, D.F.; Kravtsov, V.C.; Eckert, J.; Eubank, J.F.; Nouar, F.; Eddaoudi, M. Exceptional stability and high hydrogen uptake in hydrogen-bonded metal-organic cubes possessing ACO and AST zeolite-like topologies. *J. Am. Chem. Soc.* **2009**, *131*, 10394–10396. [[CrossRef](#)]
22. Alkordi, M.H.; Brant, J.A.; Wojtas, L.; Kravtsov, V.C.; Cairns, A.J.; Eddaoudi, M. Zeolite-like metal-organic frameworks (ZMOFs) based on the directed assembly of finite metal-organic cubes (MOCs). *J. Am. Chem. Soc.* **2009**, *131*, 17753–17755. [[CrossRef](#)] [[PubMed](#)]
23. Wang, S.; Zhao, T.; Li, G.; Wojtas, L.; Huo, Q.; Eddaoudi, M.; Liu, Y. From metal-organic squares to porous zeolite-like supramolecular assemblies. *J. Am. Chem. Soc.* **2010**, *132*, 18038–18041. [[CrossRef](#)] [[PubMed](#)]
24. Li, J.; Kan, L.; Li, J.; Liu, Y.; Eddaoudi, M. Quest for zeolite-like supramolecular assemblies: Self-assembly of metal-organic squares via directed hydrogen bonding. *Angew. Chem. Int. Ed.* **2020**, *59*, 19659–19662. [[CrossRef](#)] [[PubMed](#)]
25. Pérez-Yáñez, S.; Beobide, G.; Castillo, O.; Cepeda, J.; Luque, A.; Román, P. Structural diversity in a copper(II)/isophthalato/9-methyladenine system. From one- to three-dimensional metal-biomolecule frameworks. *Cryst. Growth Des.* **2013**, *13*, 3057–3067. [[CrossRef](#)]

26. Duan, H.; Dan, W.Y.; Fang, X.D. Zinc-coordinated MOFs complexes regulated by hydrogen bonds: Synthesis, structure and luminescence study toward broadband white-light emission. *J. Solid State Chem.* **2018**, *260*, 159–164. [[CrossRef](#)]
27. Manna, B.; Mukherjee, S.; Desai, A.V.; Sharma, S.; Krishna, R.; Ghosh, S.K. A π -electron deficient diamino-triazine functionalized MOF for selective sorption of benzene over cyclohexane. *Chem. Commun.* **2015**, *51*, 15386–15389. [[CrossRef](#)] [[PubMed](#)]
28. Ding, M.; Flaig, R.W.; Jiang, H.-L.; Yaghi, O.M. Carbon capture and conversion using metal–organic frameworks and MOF-based materials. *Chem. Soc. Rev.* **2019**, *48*, 2783–2828. [[CrossRef](#)]
29. Qiao, J.; Zhang, B.; Yu, X.; Zou, X.; Liu, X.; Zhang, L.; Liu, Y. A stable Y(III)-based amide-functionalized metal-organic framework for propane/methane separation and knoevenagel condensation. *Inorg. Chem.* **2022**, *61*, 3708–3715. [[CrossRef](#)]
30. Liao, P.Q.; Zhang, W.X.; Zhang, J.P.; Chen, X.M. Efficient purification of ethene by an ethane-trapping metal-organic framework. *Nat. Commun.* **2015**, *6*, 8697. [[CrossRef](#)]
31. Liao, P.Q.; Huang, N.Y.; Zhang, W.X.; Zhang, J.P.; Chen, X.M. Controlling guest conformation for efficient purification of butadiene. *Science* **2017**, *356*, 1193–1196. [[CrossRef](#)]
32. Bao, Z.; Xie, D.; Chang, G.; Wu, H.; Li, L.; Zhou, W.; Wang, H.; Zhang, Z.; Xing, H.; Yang, Q.; et al. Fine Tuning and specific binding sites with a porous hydrogen-bonded metal-complex framework for gas selective separations. *J. Am. Chem. Soc.* **2018**, *140*, 4596–4603. [[CrossRef](#)]
33. Li, J.; Dai, C.; Cao, Y.; Sun, X.; Li, G.; Huo, Q.; Liu, Y. Lewis basic site (LBS)-functionalized zeolite-like supramolecular assemblies (ZSAs) with high CO₂ uptake performance and highly selective CO₂/CH₄ separation. *J. Mater. Chem. A* **2017**, *5*, 21429–21434. [[CrossRef](#)]
34. Fan, W.; Zhang, X.; Kang, Z.; Liu, X.; Sun, D. Isorecticular chemistry within metal-organic frameworks for gas storage and separation. *Coord. Chem. Rev.* **2021**, *443*, 213968. [[CrossRef](#)]
35. ZareKarizi, F.; Joharian, M.; Morsali, A. Pillar-layered MOFs: Functionality, interpenetration, flexibility and applications. *J. Mater. Chem. A* **2018**, *6*, 19288–19329. [[CrossRef](#)]
36. Blatov, V.A.; Shevchenko, A.P.; Proserpio, D.M. Applied topological analysis of crystal structures with the program package ToposPro. *Cryst. Growth Des.* **2014**, *14*, 3576–3586. [[CrossRef](#)]
37. Kyprianidou, E.J.; Papaefstathiou, G.S.; Manos, M.J.; Tasiopoulos, A.J. A flexible Cd²⁺ metal organic framework with a unique (3,3,6)-connected topology, unprecedented secondary building units and single crystal to single crystal solvent exchange properties. *CrystEngComm* **2012**, *14*, 8368–8373. [[CrossRef](#)]
38. Sun, L.; Xing, H.; Xu, J.; Liang, Z.; Yu, J.; Xu, R. A novel (3,3,6)-connected luminescent metal–organic framework for sensing of nitroaromatic explosives. *Dalton Trans.* **2013**, *42*, 5508–5513. [[CrossRef](#)]
39. Suh, M.P.; Park, H.J.; Prasad, T.K.; Lim, D.W. Hydrogen storage in metal-organic frameworks. *Chem. Rev.* **2012**, *112*, 782–835. [[CrossRef](#)]
40. Myers, A.L.; Prausnitz, J.M. Thermodynamics of mixed-gas adsorption. *AIChE J.* **1965**, *11*, 121–127. [[CrossRef](#)]
41. Li, L.; Wang, X.; Liang, J.; Huang, Y.; Li, H.; Lin, Z.; Cao, R. Water-stable anionic metal-organic framework for highly selective separation of methane from natural gas and pyrolysis gas. *ACS Appl. Mater. Interfaces* **2016**, *8*, 9777–9781. [[CrossRef](#)]
42. He, Y.; Zhang, Z.; Xiang, S.; Fronczek, F.R.; Krishna, R.; Chen, B. A microporous metal-organic framework for highly selective separation of acetylene, ethylene, and ethane from methane at room temperature. *Chem. Eur. J.* **2012**, *18*, 613–619. [[CrossRef](#)]
43. Cheng, H.; Wang, Q.; Ding, M.; Gao, Y.; Xue, D.; Bai, J. Modifying a partial corn-sql layer-based (3,3,3,3,4,4)-c topological MOF by substitution of OH[−] with Cl[−] and its highly selective adsorption of C₂ hydrocarbons over CH₄. *Dalton Trans.* **2021**, *50*, 4840–4847. [[CrossRef](#)] [[PubMed](#)]
44. Tran, T.V.; Le, H.T.N.; Ha, H.Q.; Duong, X.N.T.; Nguyen, L.H.T.; Doan, T.L.H.; Nguyen, H.L.; Truong, T. A five coordination Cu(II) cluster-based MOF and its application in the synthesis of pharmaceuticals via sp³ C–H/N–H oxidative coupling. *Catal. Sci. Technol.* **2017**, *7*, 3453–3458. [[CrossRef](#)]
45. Plonka, A.M.; Chen, X.; Wang, H.; Krishna, R.; Dong, X.; Banerjee, D.; Woerner, W.R.; Han, Y.; Li, J.; Parise, J.B. Light hydrocarbon adsorption mechanisms in two calcium-based microporous metal organic frameworks. *Chem. Mat.* **2016**, *28*, 1636–1646. [[CrossRef](#)]
46. Yoon, T.-U.; Baek, S.B.; Kim, D.; Kim, E.-J.; Lee, W.-G.; Singh, B.K.; Lah, M.S.; Bae, Y.-S.; Kim, K.S. Efficient separation of C₂ hydrocarbons in a permanently porous hydrogen-bonded organic framework. *Chem. Commun.* **2018**, *54*, 9360–9363. [[CrossRef](#)] [[PubMed](#)]
47. Yang, L.; Yan, L.; Niu, W.; Feng, Y.; Fu, Q.; Zhang, S.; Zhang, Y.; Li, L.; Gu, X.; Dai, P.; et al. Adsorption in reversed order of C₂ hydrocarbons on an ultramicroporous fluorinated metal-organic framework. *Angew. Chem. Int. Ed.* **2022**, *61*, e202204046.
48. Lin, R.-B.; Wu, H.; Li, L.; Tang, X.-L.; Li, Z.; Gao, J.; Cui, H.; Zhou, W.; Chen, B. Boosting ethane/ethylene separation within isorecticular ultramicroporous metal-organic frameworks. *J. Am. Chem. Soc.* **2018**, *140*, 12940–12946. [[CrossRef](#)]
49. Li, L.; Lin, R.-B.; Krishna, R.; Li, H.; Xiang, S.; Wu, H.; Li, J.; Zhou, W.; Chen, B. Ethane/ethylene separation in a metal-organic framework with iron-peroxo sites. *Science* **2018**, *362*, 443–446. [[CrossRef](#)]
50. He, Y.; Zhang, Z.; Xiang, S.; Fronczek, F.R.; Krishna, R.; Chen, B. A robust doubly interpenetrated metal-organic framework constructed from a novel aromatic tricarboxylate for highly selective separation of small hydrocarbons. *Chem. Commun.* **2012**, *48*, 6493–6495. [[CrossRef](#)]
51. Duan, J.; Yan, R.; Qin, L.; Wang, Y.; Wen, L.; Cheng, S.; Xu, H.; Feng, P. Highly selective gaseous and liquid-phase separation over a novel cobalt(II) metal-organic framework. *ACS Appl. Mater. Interfaces* **2018**, *10*, 23009–23017. [[CrossRef](#)]

52. Liu, K.; Ma, D.; Li, B.; Li, Y.; Yao, K.; Zhang, Z.; Han, Y.; Shi, Z. High storage capacity and separation selectivity for C₂ hydrocarbons over methane in the metal-organic framework Cu-TDPAT. *J. Mater. Chem. A* **2014**, *2*, 15823–15828. [[CrossRef](#)]
53. Zhou, P.; Wang, X.; Yue, L.; Fan, L.; He, Y. A microporous MOF constructed by cross-linking helical chains for efficient purification of natural gas and ethylene. *Inorg. Chem.* **2021**, *60*, 14969–14977. [[CrossRef](#)] [[PubMed](#)]
54. Yin, Q.; Lü, J.; Li, H.-F.; Liu, T.-F.; Cao, R. Robust Microporous Porphyrin-Based Hydrogen-Bonded Organic Framework for Highly Selective Separation of C₂ Hydrocarbons versus Methane. *Cryst. Growth Des.* **2019**, *19*, 4157–4161. [[CrossRef](#)]
55. Wang, B.; Lv, X.-L.; Lv, J.; Ma, L.; Lin, R.-B.; Cui, H.; Zhang, J.; Zhang, Z.; Xiang, S.; Chen, B. A novel mesoporous hydrogen-bonded organic framework with high porosity and stability. *Chem. Commun.* **2020**, *56*, 66–69. [[CrossRef](#)]
56. Sikdar, N.; Bonakala, S.; Haldar, R.; Balasubramanian, S.; Maji, T.K. Dynamic entangled porous framework for hydrocarbon (C₂–C₃) storage, CO₂ capture, and separation. *Chem. Eur. J.* **2016**, *22*, 6059–6070. [[CrossRef](#)]
57. Bruker. *SAINTE, V8.34A*; Bruker AXS Inc.: Madison, WI, USA, 2013.
58. Krause, L.; Herbst-Irmer, R.; Sheldrick, G.M.; Stalke, D. Comparison of silver and molybdenum microfocus X-ray sources for single-crystal structure determination. *J. Appl. Crystallogr.* **2015**, *48*, 3–10. [[CrossRef](#)] [[PubMed](#)]
59. Sheldrick, G. SHELXT—Integrated space-group and crystal-structure determination. *Acta Crystallogr. Sect. A* **2015**, *71*, 3–8. [[CrossRef](#)]
60. Sheldrick, G. Crystal structure refinement with SHELXL. *Acta Crystallogr. Sect. C* **2015**, *71*, 3–8. [[CrossRef](#)]
61. Groom, C.R.; Bruno, I.J.; Lightfoot, M.P.; Ward, S.C. The Cambridge Structural Database. *Acta Crystallogr. Sect. B* **2016**, *72*, 171–179. [[CrossRef](#)]
62. Kratzert, D. FinalCif, V104. Available online: <https://dkratzert.de/finalcif.html> (accessed on 20 April 2020).
63. Kresse, G.; Furthmüller, J. Efficiency of ab-initio total energy calculations for metals and semiconductors using a plane-wave basis set. *Comput. Mater. Sci.* **1996**, *6*, 15–50. [[CrossRef](#)]
64. Blöchl, P.E. Projector augmented-wave method. *Phys. Rev. B* **1994**, *50*, 17953–17979. [[CrossRef](#)] [[PubMed](#)]
65. Kresse, G.; Joubert, D. From ultrasoft pseudopotentials to the projector augmented-wave method. *Phys. Rev. B* **1999**, *59*, 1758–1775. [[CrossRef](#)]
66. Perdew, J.P.; Burke, K.; Ernzerhof, M. Generalized gradient approximation made simple. *Phys. Rev. Lett.* **1996**, *77*, 3865–3868. [[CrossRef](#)] [[PubMed](#)]
67. Monkhorst, H.J.; Pack, J.D. Special points for Brillouin-zone integrations. *Phys. Rev. B* **1976**, *13*, 5188–5192. [[CrossRef](#)]
68. Grimme, S.; Antony, J.; Ehrlich, S.; Krieg, H. A consistent and accurate ab initio parametrization of density functional dispersion correction (DFT-D) for the 94 elements H-Pu. *J. Chem. Phys.* **2010**, *132*, 154104. [[CrossRef](#)] [[PubMed](#)]
69. Grimme, S.; Ehrlich, S.; Goerigk, L. Effect of the damping function in dispersion corrected density functional theory. *J. Comput. Chem.* **2011**, *32*, 1456–1465. [[CrossRef](#)]
70. Zhang, X.J.; Shang, C.; Liu, Z.P. Double-ended surface walking method for pathway building and transition state location of complex reactions. *J. Chem. Theory Comput.* **2013**, *9*, 5745–5753. [[CrossRef](#)]
71. Wei, G.F.; Liu, Z.P. Restructuring and hydrogen evolution on Pt nanoparticle. *Chem. Sci.* **2015**, *6*, 1485–1490. [[CrossRef](#)]

Disclaimer/Publisher’s Note: The statements, opinions and data contained in all publications are solely those of the individual author(s) and contributor(s) and not of MDPI and/or the editor(s). MDPI and/or the editor(s) disclaim responsibility for any injury to people or property resulting from any ideas, methods, instructions or products referred to in the content.